Study on Four-Dimensional Evolution of Concentric Traveling Ionospheric Disturbances After Falcon 9 Rocket Launch Using Ionospheric Tomography

Yutian Chen, Dongjie Yue, and Changzhi Zhai

***Abstract*—The ionospheric disturbances induced by the Falcon 9 rocket launch on 17 January 2016 were reconstructed by three-dimensional computerized ionospheric tomography using observations from the North American global navigation satellite system networks. The results showed that concentric traveling ionospheric disturbances (CTIDs) occurred ∼18 min after the rocket launch and were remarkable at 200–300 km altitudes. The vertical phase velocities of the CTIDs were consistent with the inclinations of the U-shaped structures. At specific azimuth directions of 350°, 30°, and 105°, the estimated vertical phase velocities between 100 and 200 km altitudes were ∼222.2, ∼208.3, and ∼242.4 m/s, respectively. When the CTIDs propagated upward to 400–500 km altitudes, their vertical velocities increased to ∼566.7, ∼966.7, and ∼944.4 m/s. CTIDs traveling northward (azimuths 350°, 30°) had periods of ∼11 min. At 200 and 300 km altitudes, their horizontal phase velocities were ∼309.9–323.3 and ∼309.4–330.9 m/s, respectively, with horizontal wavelengths of ∼204.5–213.4 and ∼204.2–218.4 km. In contrast, CTIDs propagating eastward (azimuth 105°) displayed a period of ∼15 min. At 200 and 300 km altitudes, their horizontal phase velocities were ∼223.2 and ∼241.1 m/s, respectively, with horizontal wavelengths of ∼200.9 and ∼217.0 km. These CTIDs propagation characteristics agreed well with the theory of gravity waves.**

***Index Terms*—Concentric traveling ionospheric disturbances (CTIDs), Falcon rocket, global navigation satellite system (GNSS), ionosphere, three-dimensional computerized ionospheric tomography (3-DCIT).**

I. Introduction

THE transport of momentum and energy in the lower atmosphere can affect the ionosphere, such as the hit of the rising plume on the top of the troposphere in meteorological events [1], [2], [3], [4], [5], and atmospheric wave modes excited by the coupling of the hydrosphere and lithosphere with the lower atmosphere in geological disasters [6], [7], [8]. These energies can leak from the troposphere to the thermosphere at certain frequencies to influence the distribution of electron density (Ne) and excite ripples with different scales. Thus, the traveling ionospheric disturbances (TIDs) are considered as the manifestation of the dynamics induced by propagating thermospheric waves [9]. In addition to natural events, human activities, such as rocket and spacecraft launches, can also generate strong exhaust plumes during their ascent that excite atmospheric acoustic disturbances and induce TIDs in the ionosphere [10], [11].

Early studies on the impact of rocket launch processes on the ionosphere primarily relied on sparse land-based observation sequences to probe perturbation information. For instance, during the Apollo 14 launch, the vertically detected plasma frequencies from Red Hill Station demonstrated continuous compression or undulation [10]. Noble [12] observed long-distance propagation TIDs with periods of 15–75 min in the ionosphere during the launch of the STS-4 space shuttle using the incoherent scattering radar. Jacobson and Carlos [13] employed Doppler sounders to observe acoustic and buoyancy waves resulting from the initial explosion and subsequent buoyancy rise, respectively, during three space shuttle launch events from 1990 to 1991. Li et al. [14] investigated the effect of shock waves from the main engine burn of a space shuttle on the ionospheric electron density using line-of-sights (LOSs) from a very-long-baseline interferometer. Calais and Minster [11] first used total electron content (TEC) sequences obtained from global positioning system (GPS) observations during the STS-58 space shuttle launch to report the GWs induced disturbances lasting 35 min with period of less than 10 min. This demonstrated the feasibility of GPS observations in detecting ionospheric disturbances induced by such events. However, these studies only revealed the linear and spectrum characteristics of the disturbance due to the limitations of stations and observation LOSs, and the spatial characteristics of the disturbance are difficult to be described in detail.

In recent years, with the development of worldwide global navigation satellite system (GNSS) receiver networks, the ionospheric sounding technology based on mutifrequency observation can accurately acquire ionospheric TEC and reflect the spatial characteristics of the ionosphere by rich ionospheric pierce points (IPPs) [15], [16], [17]. Simultaneously, the increasing number of rocket launch activities provided opportunities for studying the induced ionospheric disturbances [18], [19], [20]. Ding et al. [21] used China's dense GNSS networks to report the ionospheric response to the Shenzhou-10 launch on 11 June 2013, and detected long-range propagating shock waves

Manuscript received 17 June 2023; revised 11 October 2023; accepted 28 October 2023. Date of publication 1 November 2023; date of current version 23 November 2023. This work was supported in part by the National Natural Science Foundation of China under Grant 42104009, and in part by the China Postdoctoral Science Foundation under Grant 2022M720988. *(Corresponding author: Dongjie Yue.)*

The authors are with the School of Earth Sciences and Engineering, Hohai University, Nanjing 211100, China (e-mail: chenyt@hhu.edu.cn; yuedongjie@hhu.edu.cn; czzhai@hhu.edu.cn).

Digital Object Identifier 10.1109/JSTARS.2023.3329203

and acoustic waves. Kakinami et al. [22] observed V-shaped ionospheric disturbances propagating at 1.8–2.6 km/s caused by North Korea's missile launch on 12 December 2012 using a nearby GNSS network. In study of Lin et al. [23], a similar V-shaped feature was also captured ∼5 min after the Falcon 9 rocket launch on 17 January 2016, and remarkable concentric traveling ionospheric disturbances (CTIDs) were observed in the subsequent evolution. Similarly, Chou et al. [24] observed northward propagating TIDs with a period of ∼6–8 min after the launch of the SpaceX Falcon Heavy rocket on 6 February 2018, with horizontal phase velocities of ∼420–488 and horizontal wavelengths of ∼164–240 km. These studies showed nice wave-like disturbances, but the vertical propagation and 3-D structure of ionospheric disturbances were still not well described since the limitations of TEC by the single-layer model (SLM). Furthermore, synchronous information on the horizontal and vertical propagation of TIDs is essential for understanding the relationships between atmospheric wave modes and TIDs, as well as ion-neutral coupling processes.

Three-dimensional computerized ionospheric tomography (3-DCIT) can use the slant TEC (STEC) information contained in the GNSS signals to reconstruct the 3-D electron density distribution and provide critical spatial–temporal features on the evolution of ionospheric disturbances, compensating for the lack of vertical description by SLM [25], [26], [27]. For example, Ssessanga et al. [28] used ionospheric tomography for the first time to quantify the horizontal and vertical structure of the electron density during nighttime medium-scale traveling ionospheric disturbances. In the investigations of 2011 Japan Tohoku earthquake [29] and the 2015 Nepal earthquake [30], ionospheric tomography was employed to determine the altitudes and 3-D propagation parameters of earthquake induced ionospheric disturbances, enabling a better understanding of the lithosphere–atmosphere–ionosphere coupling processes. Moreover, Chen et al. [31] reported detailed information on the horizontal and vertical evolutions of CTIDs excited by GWs during Hurricane Matthew, demonstrating ionospheric tomography as an effective tool for ionospheric disturbance detection.

This article employed 3-DCIT with detrended STEC (dSTEC) to reconstruct ionospheric disturbances that were induced by the Falcon 9 rocket launch on 17 January 2016. The reliability of the method was verified. The 3-D characteristics of the disturbances were analyzed, including their propagation velocities and wavelengths in different directions and altitude planes. In addition, the generation and evolution of disturbances were discussed in conjunction with the theory of GWs.

II. Theory and Methodology

The STEC observations are obtained by precise point positioning technology [15], [32]. They can be described as the integral of electron density along the LOS path between a satellite and a receiver. When the ionosphere is divided into voxels (i.e., grid cells limited by longitude × latitude × altitude) with uniform electron density [29], the STEC can be expressed as a polynomial function of the voxel intercepts, and formulated as a system of linear equations with the matrix form, as follows:

$$Y_{m\times\mathbf{1}}^{\mathrm{STEC}} = A_{m\times n}\cdot X_{n\times\mathbf{1}}^{\mathrm{Ne}} + \varepsilon_{m\times\mathbf{1}} \tag{1}$$

where m and n are the number of STEC and voxels, respectively; $Y_{m\times\mathbf{1}}^{\mathrm{STEC}}$ indicates the STEC vector; $\boldsymbol{A_{m\times n}}$ represents the intercept matrix; vector $X_{n\times\mathbf{1}}^{\mathrm{Ne}}$ contains the electron density of voxels; and $\varepsilon_{m\times\mathbf{1}}$ is the error vector of measurements.

The Butterworth bandpass filter is used to remove the ionospheric background trend to obtain the dSTEC sequences that reflect ionospheric disturbances [21], [33], [34]. If dSTEC can be represented as the integral of electron density disturbances (dNe), then (1) can be modified as follows:

$$Y_{m\times\mathbf{1}}^{\mathrm{dSTEC}} = A_{m\times n}\cdot X_{n\times\mathbf{1}}^{\mathrm{dNe}} + d\varepsilon_{m\times\mathbf{1}} \tag{2}$$

where $Y_{m\times\mathbf{1}}^{\mathrm{dSTEC}}$ stands for the dSTEC vector; $X_{n\times\mathbf{1}}^{\mathrm{dNe}}$ represents the distribution of dNe in voxels; and $\boldsymbol{d}\varepsilon_{\mathbf{m}\times\mathbf{1}}$ is the error vector of dSTEC observations.

In addition, the improved constrained simultaneous iterative reconstruction technique (ICSIRT) is used to resolve (2) to obtain the dNe of the voxel iteratively [27]. This algorithm can use the average of all LOS corrections in a voxel to modify each voxel in an iteration, which avoids the influence of LOS ordering on correction and makes the amount of correction received by voxels more statistical. In the $(k+1)$th iteration, the jth voxel is modified as follows:

$$x_j^{(k+1)} = x_j^{(k)} + \frac{1}{P}\sum_{i=1}^{P}\lambda\cdot\left(y_i - \sum_{q=1}^{Q}A_{i,q}\cdot x_q^{(k)}\right) \times \frac{x_j^{(k)}}{\sum_{q=1}^{Q}A_{i,q}\cdot x_q^{(k)}} \tag{3}$$

where k is the iteration number; $x_j^{(k)}$ is the electron density in the jth voxel after the kth iteration; P indicates the number of LOSs traversing the jth voxel; y_i is the dSTEC along the ith LOS; Q stands for the number of voxels traversed by the ith LOS; $A_{i,q}$ represents the intercept of the ith LOS in the qth voxel; and λ is the iteration relaxation factor defined between 0 and 1.

In this article, excessive iterations are not conducive to the reconstruction of dNe due to its small amplitude. Conversely, a larger relaxation factor helps in preserving the perturbation features more effectively. Therefore, the number of iterations (k) is 10 and the relaxation factor (λ) is set as 1. The ionosphere of the western continental USA (25–45°N, 130–110°W) is reconstructed using voxels with a resolution of 0.25° × 0.25° × 10 km and the NeQuick2 model is used for dNe assignment.

III. Observations

A. GNSS Observations

Fig. 1 presents the ionosphere's reconstruction region adjacent the launch site Vandenberg Air Force Base (34.63°N, 120.61°W, California, USA). To explore the ionospheric oscillations that ensued following the launch of the Falcon 9 rocket on 17 January 2016, a comprehensive analysis was conducted employing data from more than 1200 GNSS stations located within this zone. The rinex data were gathered by the GNSS

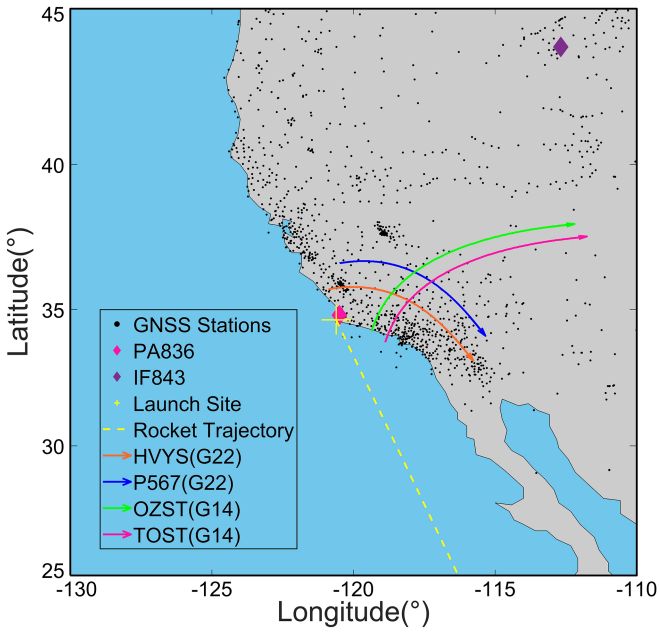

Fig. 1. Distribution of GNSS stations in the reconstructed region is marked with black dots; the ionosondes PA836 and IF843 are marked with magenta and purple diamonds, respectively; the four arrows indicate the IPP trajectories; the yellow cross marker and the yellow dashed line indicate the rocket launch site and the rocket trajectory, respectively.

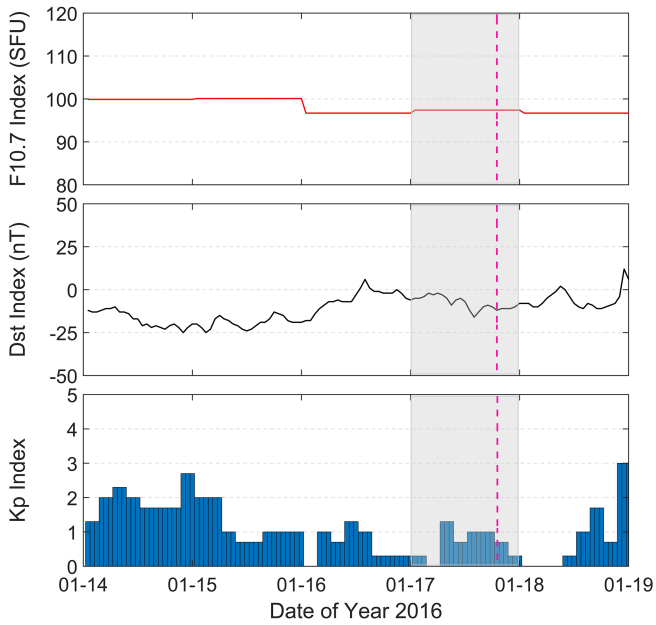

Fig. 2. F10.7, Dst, and *Kp* indices from 14 to 18 January 2016. The shadows mark the geomagnetic indices on the day of the rocket launch, while the magenta dashed lines indicate the moment of the rocket launch.

network of the National Oceanic and Atmospheric Administration (https://geodesy.noaa.gov/CORS) and the Scripps Orbit and Permanent Array Center (ftp://garner.ucsd.edu), enabling the calculation of STEC with a time resolution of 30 s. The ionosphere height was fixed at 350 km altitude and the LOS elevation angle was limited to 30° to mitigate the impact of multipath propagation. Four consecutive IPP trajectories were analyzed to determine the frequency range of ionospheric disturbances, and two ionosondes (PA836, IF843) were utilized to provide electron density profiles.

B. Solar and Geomagnetic Conditions

Fig. 2 shows the geomagnetic and solar activity indexes from 14 to 18 January 2016. The rocket launch day is indicated by a shadow, and the launch time (18:42 UT) is marked by a magenta dashed line. During this period, the F10.7 index remained relatively constant, the Dst index consistently exceeded −25 nT, and *Kp* values consistently remained below 3. Significantly, on the day of the rocket launch, the *Kp* index exhibited values below 2, indicating a stable solar-terrestrial environment with no noticeable impacts on the ionosphere.

IV. Results

A. GNSS dSTEC Sequences

Fig. 3 depicts the detrending process of the STEC sequences from the four IPP trajectories shown in Fig. 1. The time–frequency relationships corresponding to the STEC sequences are obtained using the wavelet transform [31], [35]. The results of spectrum analysis show that the significant power enhancement occurs at 19:00–19:30 UT, slightly later than the launch time. This delay is due to the time required for energy transfer from the lower atmosphere to the ionosphere and its impact on the electron density distribution [21], [24]. The amplitude of the ionospheric disturbance ranges from 0.15 to 0.25 TECU (1 TECU $= 10^{16}$ el/m^2). It appears within the frequency range of 1–2 mHz and has negligible extension to other frequency domains. The dSTEC sequences clearly display wave-like characteristics, which may be caused by the atmospheric waves induced by the rocket launch.

B. 3-DCIT Reliability Verification

As shown in Fig. 4, the electron density profiles provided by ionosondes PA836 and IF843 are used to verify the dependability of the ICSIRT. The hmF2 height obtained by the ICSIRT is ∼250 km, which is highly consistent with the ionosonde observations. The reconstructed electron density profiles with a peak of ∼6–8 $\times$ 10^{11} el/m^3, which agree well with the electron density values probed by the ionosondes, indicating the good reliability of the algorithm. In addition, the large geographical span of the two ionosonde locations suggests that ICSIRT has good applicability in the reconstructed region.

To further validate the reliability of dNe, the voxels' dNe along the LOS are used to reconstruct dSTEC in the path. In contrast to 3-DCIT, which utilizes the intercepts of multiple LOSs within a voxel to obtain the dNe distribution, this method employs the dNe values of voxels along the LOS to invert dSTEC. Due to a completely different mapping relationship, it can be used to verify the accuracy of dNe contained within the voxels.

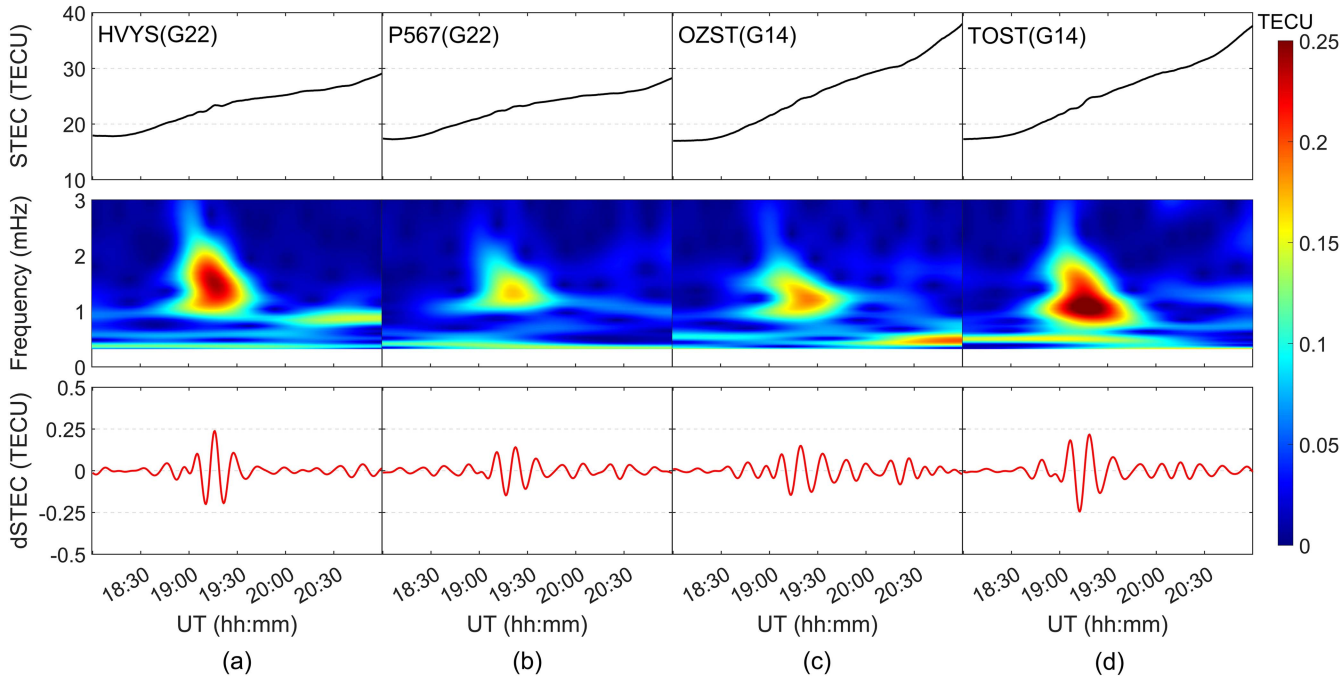

Fig. 3. Detrending process of STEC sequences. The columns from left to right are the results of GNSS receivers and corresponding satellite observations: (a) Sat.G22 tracked by HVYS, (b) Sat.G22 tracked by P567, (c) Sat.G14 tracked by OZST, and (d) Sat.G14 tracked by TOST. Top panel: original STEC sequences; middle panel: STEC spectrum via wavelet transform; bottom panel: dSTEC values obtained from a 1-2 mHz Butterworth bandpass filter.

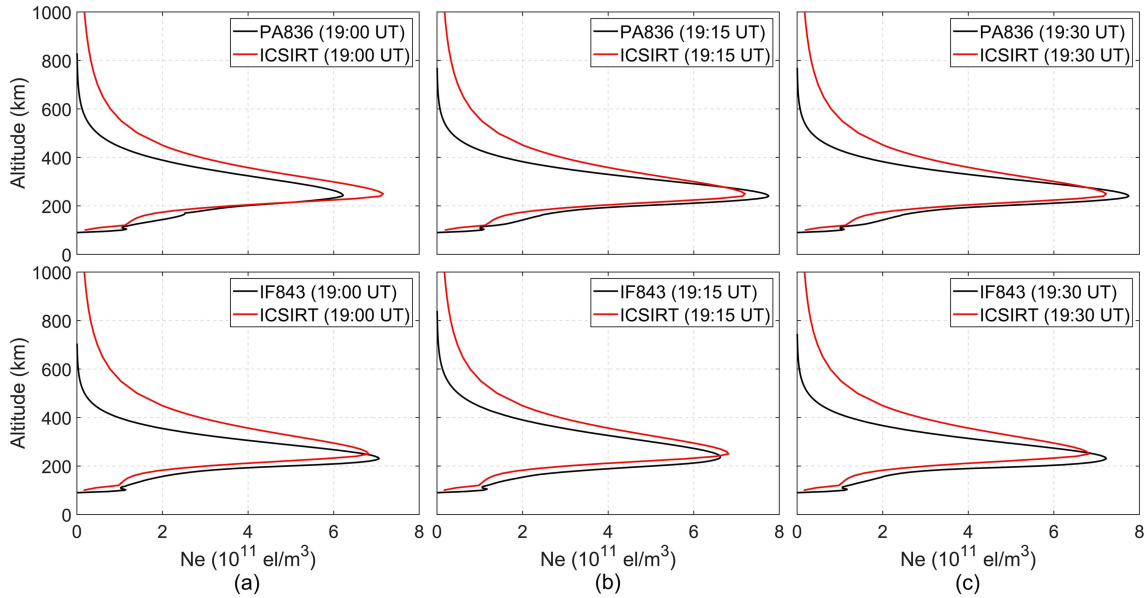

Fig. 4. Comparison between electron density profiles obtained by ionosondes PA836, IF843, and ICSIRT at (a) 19:00 UT, (b) 19:15 UT, and (c) 19:30 UT. Red lines represent the reconstructed electron density profiles, and black lines represent observations of the ionosondes.

Due to significant variations in the cutoff angles, the LOSs of satellite G14, as well as other satellites, only contribute to the reconstruction during certain moments. Thus, Fig. 5(a) exclusively compares the detected dSTEC and CIT reconstructed dSTEC (CIT–dSTEC) sequences for the satellite G22. The difference between CIT–dSTEC and the dSTEC is small, and it can well reflect the wave-like characteristics of the disturbances between 19:00 UT and 19:30 UT. This is crucial for capturing the positive and negative phases of the TIDs. Fig. 5(b) presents the statistical results of the bias between CIT–dSTEC and dSTEC for all LOSs from 18:00 to 21:00 UT. The bias values exhibit a nice Normal distribution, mainly concentrated within ± 0.05 TECU. The root mean square error [36] is calculated as 0.052 TECU, which is relatively small compared to the perturbation amplitude of 0.25

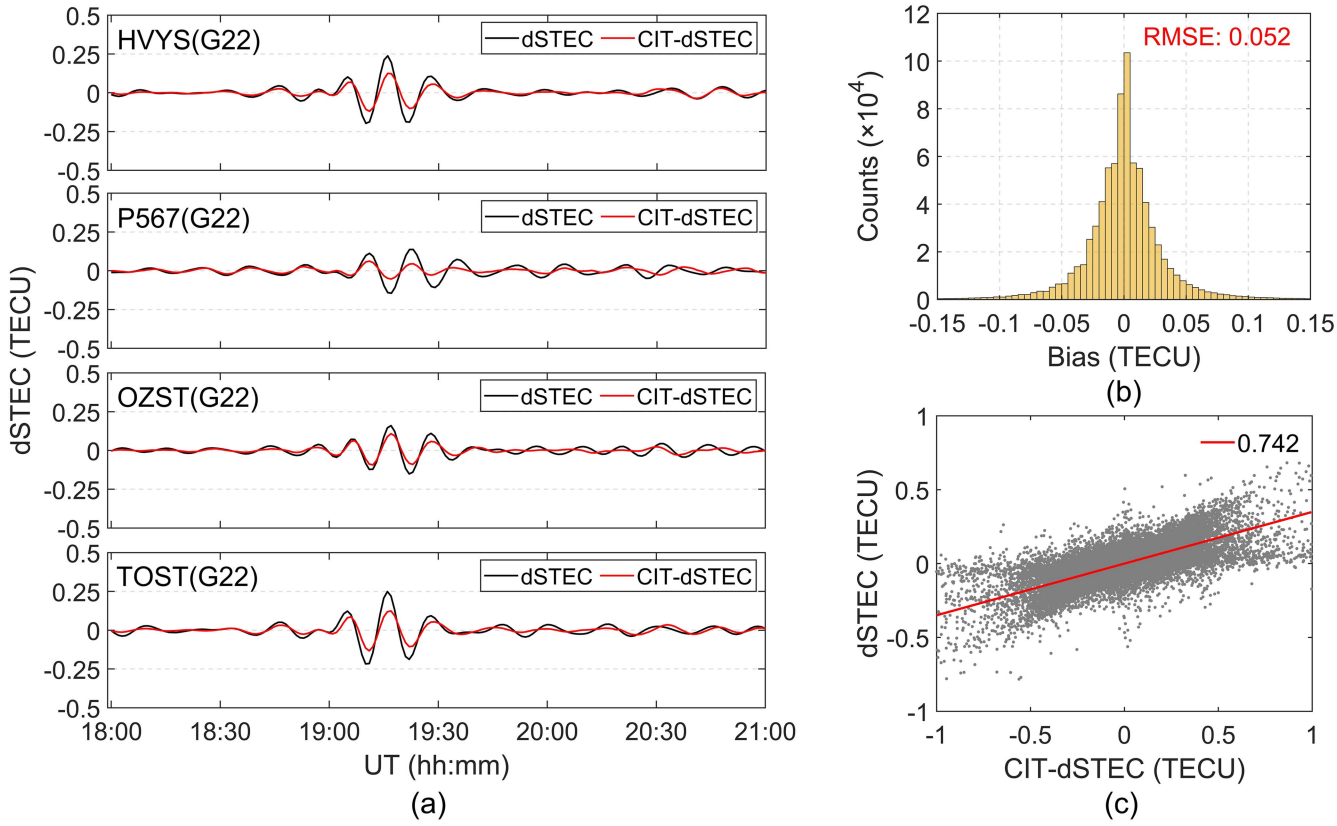

Fig. 5. (a) Comparison between the observed dSTEC and the CIT reconstructed dSTEC (CIT–dSTEC); (b) histogram of bias statistics between dSTEC and CIT–dSTEC; and (c) correlation plot between dSTEC and CIT–dSTEC.

TECU. In addition, the Pearson correlation coefficient [17] in Fig. 5(c) achieves 0.742, indicating a strong correlation between CIT–dSTEC and actual detection results. These statistics show that 3-DCIT can effectively reflect the ionospheric disturbances before and after the Falcon 9 rocket launch, and can be used to detect the 3-D characteristics of TIDs.

C. 4-D Evolution of CTIDs

Fig. 6 exhibits dNe slices at altitudes ranging from 100 to 400 km, derived from ionospheric tomography results that involve dSTEC obtained from a 1–2 mHz bandpass filter. The positive and negative phases of ionospheric disturbances appear at 100 km altitude and tend to fade away at 400 km altitude. These disturbances exhibit the largest amplitude of $\sim 0.03 \times 10^{11}$ el/m^3 at 200 km altitude and display perfect concentric rings (i.e., CTIDs). Specifically, at 19:15 UT, the CTIDs are most remarkable and can propagate northward to regions beyond 40°N, while the eastward propagating CTIDs rapidly dissipate. Similar horizontal structures were captured in some meteorological [33], [37] and geological [38] events and considered to be dominated by atmospheric gravity waves (GWs). Furthermore, it is worth noting that no apparent wave-like structures were captured on the 100 km altitude slice at 19:25 UT, suggesting that the excitation source in the lower atmosphere may have dissipated. As shown in Lin et al. [23], the Falcon 9 rocket reached an altitude of 200 km just 6 min after launch.

To investigate the spatiotemporal evolution of the CTIDs, the ionosphere in the reconstructed region is sliced along three directions, as depicted in Fig. 7. These directions with azimuth angles of 350°, 30°, and 105° are defined with respect to the reference point (−120, 33), which locate near the rocket trajectory and approximately at the center of the CTIDs. The selection of these profiles considers the angles between the propagation directions of TIDs and the Earth's magnetic field lines. They are chosen to ensure remarkable disturbances are detected while maximizing the differences in angles with respect to the magnetic field. The dashed line represents an equidistant line 600 km away from the reference point, as the CTIDs start to break beyond this distance. The white dots are vertical profile points placed at the three directions abovementioned to record the vertical propagation parameters of CTIDs at 100–800 km altitudes.

In practical calculations, if the reference point has coordinates (X_o, Y_o) and any point along a profile is denoted as (X_i, Y_i), then its distance from the reference point can be indicated as $D = (R+H) * \arccos(\sin(Y_o) * \sin(Y_i) + \cos(Y_o) * \cos(Y_i) * \cos(X_i - X_o))$, where R is the Earth's radius and H is the altitude of the point. Therefore, the horizontal phase velocity of the CITDs, $V_h = \Delta D / \Delta t$, where ΔD represents the change in distance relative to the reference point during the time interval Δt. Similarly, the vertical phase velocity, $V_z = \Delta H/\Delta t$, where ΔH represents the change in height within Δt. The disturbance wavelength, $\lambda = T * V$, where T is the disturbance period (i.e., the duration of a set of positive and negative disturbances).

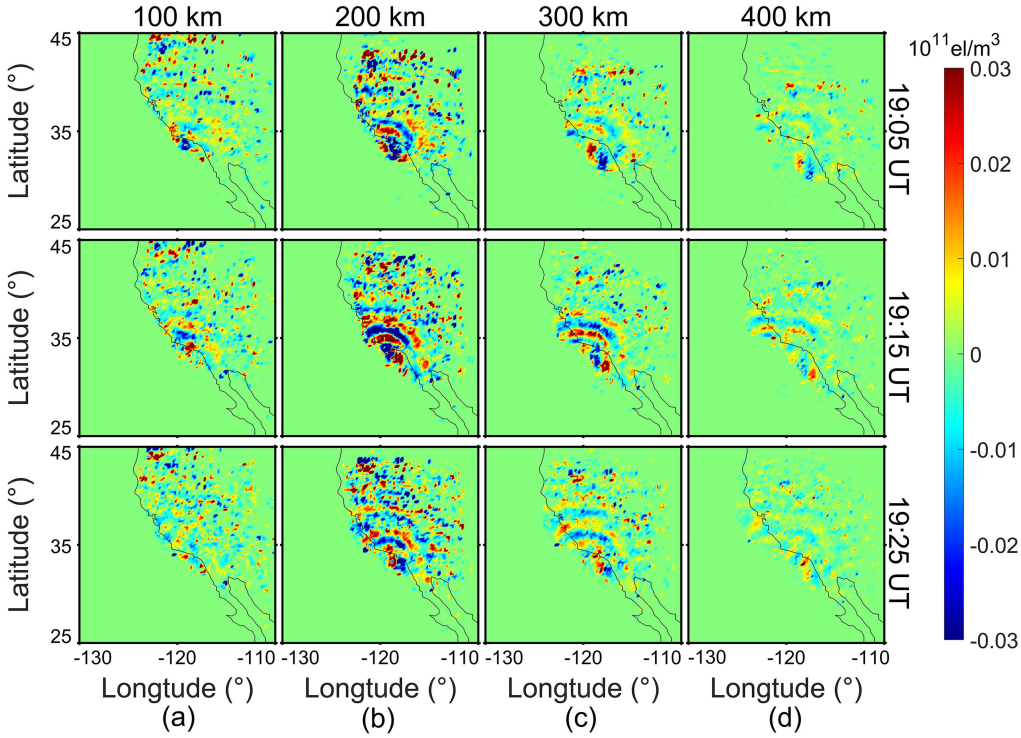

Fig. 6. Horizontal slices of reconstructed dNe at altitudes of (a) 100 km, (b) 200 km, (c) 300 km, and (d) 400 km. The top row shows slices at 19:05 UT, the middle row at 19:15 UT, and the bottom row at 19:25 UT.

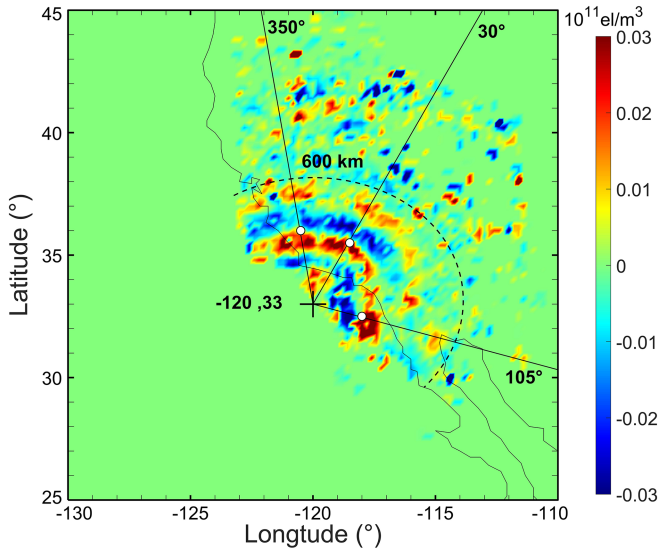

Fig. 7. Schematic diagram of ionospheric dNe profiles. The cross marker denotes the reference point (−120, 33); the solid lines represent selected azimuths at 350°, 30°, and 105°; the dashed line represents an equidistant line with a radius of 600 km centered on the reference point.

The time–distance–disturbance relationships at altitudes of 200 and 300 km are analyzed, as illustrated in Fig. 8. The results reveal that while the phase velocities and wavelengths of the disturbances show slight variations in the same direction at different altitude slices, the eastward and northward propagating CTIDs exhibit great differences. For instance, CTIDs propagating in the 30° direction exhibit comparable horizontal phase velocities and wavelengths at 200 km (309.9 m/s, 204.5 km) and 300 km (309.4 m/s, 204.2 km) altitudes. However, the horizontal phase velocities of northward propagating CTIDs are significantly larger than those of eastward propagating CTIDs. Especially, CTIDs in the 350° direction demonstrate horizontal phase velocities of 323.3–330.9 m/s and horizontal wavelengths of 213.4–218.4 km, which are much greater than those in the 105° direction with horizontal phase velocities of 223.2–241.1 m/s and horizontal wavelengths of 200.9–217.0 km. In addition, these horizontal phase velocities are comparable to those detected by Lin et al. [23] using subionospheric points (SIPs) at an altitude of 200 km (∼241–348 m/s).

Fig. 9 gives the distance–altitude profiles of ionospheric dNe along the three directions at 19:15 UT. The CTID's positive and negative phases are concentrated between altitudes of 100–500 km. The CTIDs propagating northward (Az: 350° and 30°) can travel to 600 km away from the reference point, with significant phase disturbances at ∼200–400 km. Nevertheless, the eastward propagating CTIDs reach only ∼400 km from the reference point, with significant phase disturbances at ∼50–250 km. The black dashed lines illustrate the vertical structure of the CTIDs. Unlike the upside-down cone shape reported in some studies [29], [39], these CTIDs exhibit a U-shape with the inclination increases with altitude. This phenomenon may be due to different phase velocities of GWs at different altitudes. As shown in Fig. 9, the inclination angles of the CTIDs for the three directions (Az: 350°, 30°, and 105°) are ∼28.8°–57.9°, 12.5°–72.2°, and 29.1°–68.9°, respectively.

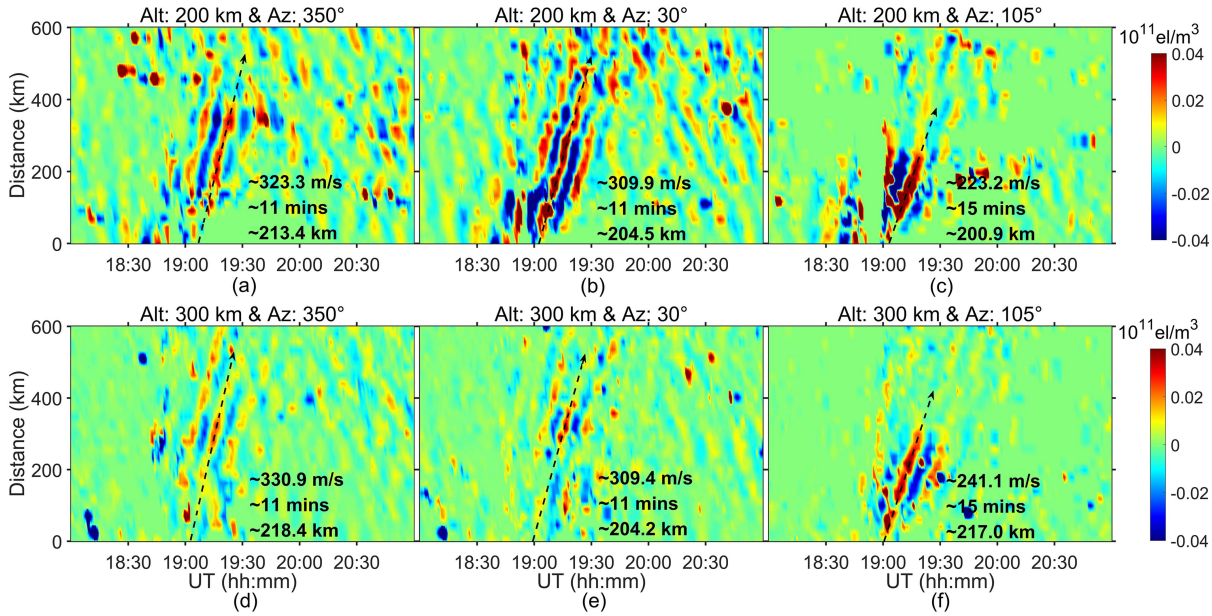

Fig. 8. Time–distance–dNe plots at 200 km altitude for azimuths: (a) 350°, (b) 30°, (c) 105°, and at 300 km altitude for azimuths; (d) 350°, (e) 30°, and (f) 105°. The slope of dashed arrows shows the horizontal phase velocities of the disturbances, with corresponding periods and horizontal wavelengths indicated.

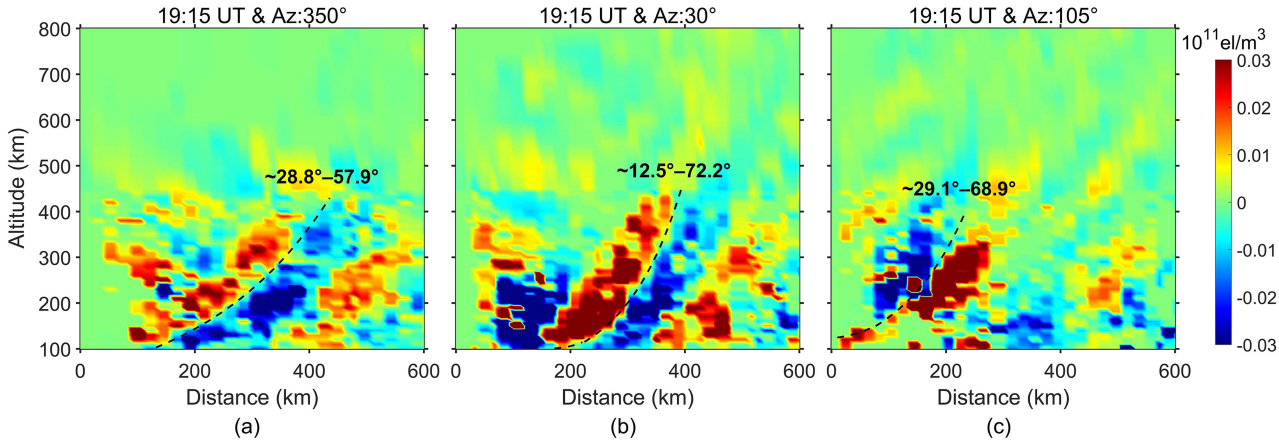

Fig. 9. Vertical dNe slices in three azimuthal directions: (a) 350°, (b) 30°, and (c) 105° at 19:15 UT. The dashed lines indicate vertical disturbance structures and their altitude-dependent inclinations.

Fig. 10 shows the time–altitude–disturbance relationships recorded by the profile points in the three abovementioned directions. The CTIDs appear during 19:00–20:00 UT, showing downward phases. This is because GWs induced TIDs have a longer propagation time at higher altitudes and are captured earlier by the vertical profile points. Notably, the phase velocities of these disturbances are smaller at lower altitudes and increase at higher altitudes. For instance, at the profile point −118.5, 35 in the direction of azimuth 30° (i.e., −188.5, 35 & Az: 30°), the vertical phase velocity of CTIDs is ∼208.3 m/s at altitudes of 100–200 km and reaches ∼977.6 m/s at 400–500 km altitudes. When combined with the inclination information provided in Fig. 9, it appears that the vertical phase velocities of CTIDs increase with their vertical inclination angles. In addition, the northward-propagating CTIDs (profiles at −120.5, 36, and −118.5, 35) have an intrinsic period of ∼11 min, while the eastward-propagating CTIDs (profiles at −118, 32.5) exhibit a period of ∼15 min, with their corresponding vertical wavelengths being ∼137.5–657.8 and ∼218.2–849.9 km, respectively.

V. Discussions

The interaction between the rocket's exhaust plume and the ionospheric plasma after a rocket launch through dissociative recombination can induce ionospheric depletion, which contributes to the formation of ionospheric holes [40], [41]. The ionospheric holes exhibit significant differences in scale, magnitude, and period compared to TIDs induced by GWs. On 16 January 2016, Savastano et al. [42] detected remarkable ionospheric holes using geosynchronous Earth orbit satellites after the Falcon 9 rocket launch, with the TEC decreased ∼6 TECU.

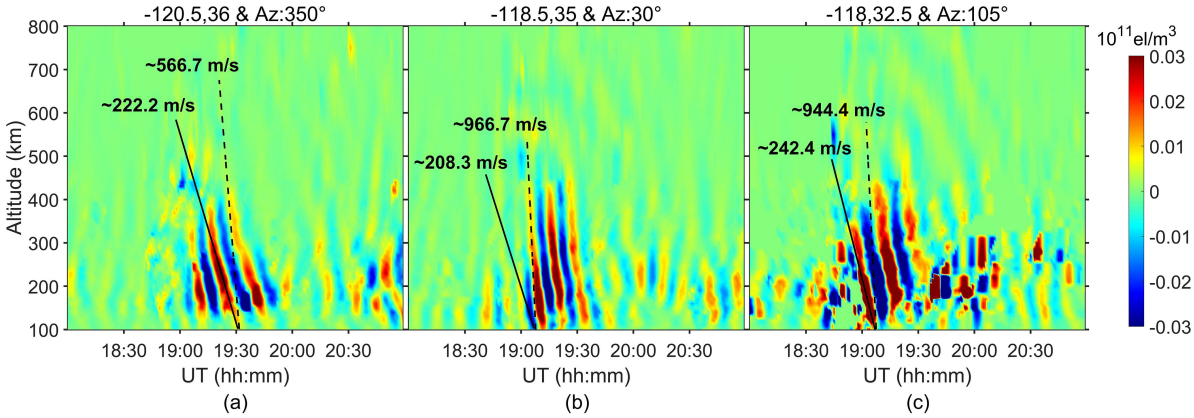

Fig. 10. Vertical phase velocities of dNe at three profile points: (a) −120.5°, 36°, (b) −118.5°, 35°, and (c) −118°, 32.5°. The solid lines indicate the vertical phase velocities of disturbances at altitudes between 100 and 200 km, and the dashed lines indicate the vertical phase velocities between 400 and 500 km altitudes.

However, spectrum analysis in Fig. 3 indicates that the amplitude of CTIDs induced by GWs is ∼0.25 TECU, distinguishing them from the impact of ionospheric holes. Furthermore, the TEC drop of ionospheric hole can last for hours, which is much longer than the period of the TIDs in this event. Therefore, the 3-DCIT reconstruction results did not capture ionospheric holes after the rocket launch.

The magnetic declination in the west coast of the USA is ∼10°, inclined downward at ∼60°. The directions of 350° and 30° azimuths are at a smaller angle to the Earth's magnetic field lines than that of 105° azimuth direction. Due to the high conductivity along the Earth's magnetic field lines, electrons and ions in the ionosphere can propagate rapidly along the magnetic field lines, while the propagation perpendicular to the magnetic field lines is much more difficult [43]. This resulted in the northward propagating CTIDs taking faster horizontal phase velocities and traveling further away than those propagating eastwards. Similarly, following the eruption of the Tonga volcano in 2022, TEC observations captured much greater horizontal phase velocities of TIDs over New Zealand than Australia due to the excellent conductivity parallel to the direction of the Earth's magnetic field [34].

Generally, when initial GWs have long wavelengths and weak amplitudes, and are weakly filtered by background winds, GWs-excited TIDs can exhibit a concentric ring structure in the ionosphere [44]. Otherwise, they tend to dissipate in the mesosphere and lower thermosphere (MLT). For example, CTIDs induced by Typhoon Meranti had an amplitude of ∼0.2 TECU and horizontal wavelengths of ∼160–200 km [33], and Hurricane Matthew generated CTIDs with an amplitude of ∼0.15 TECU and a horizontal wavelength of ∼276 km [31]. In the current event, the amplitudes and horizontal wavelengths of the ionospheric disturbances excited by the Falcon rocket were comparable to those in the above cases, allowing for the formation of concentric ring structures. Notably, the intrinsic periods of northward propagating CITDs differ from those of eastward propagating CTIDs, suggesting distinct excitation sources. Although the ignition of the second-stage rocket may be a contributing factor [23], it is still necessary to consider the potential role of secondary waves in the CTID structure induced by the acceleration of neutral wind due to local body forces [45], [46].

Unlike the SIPs at 200 km altitude adopted by Lin et al. [23], the ionospheric SLM is generally set as 300–450 km altitudes [47], [48]. Fig. 11 shows the vertical TEC disturbances (dVTEC) on the IPPs at 350 km altitude obtained by satellites G14 and G22. The time–distance–disturbance relationships are relative to the reference point (−120, 33). At ∼19:00–19:30 UT, remarkable ionospheric disturbances are captured at ∼200–400 km away from the reference point, which is consistent with the dNe reconstruction results in Fig. 8. The SLM is influenced by the Earth's curvature radius. When dSTEC is projected as dVTEC, TIDs at higher altitudes propagate over longer distances, leading to a larger estimated horizontal phase velocity. This is due to the intrinsic period of GWs remaining constant after excitation. Therefore, in this article, the horizontal phase velocities of CTIDs identified by dVTEC are slightly faster than those observed in the dNe slices at 200 and 300 km altitudes. However, the altitude of the F2 layer (hmF2) is actually ∼250 km (cf. electron density profiles in Fig. 4), and the SLM overestimates the horizontal phase velocity of the CTIDs, resulting in marginally longer horizontal wavelengths. The 3-DCIT can make slices at different ionospheric heights to compensate for the limitations of SLM. In Fig. 8, the horizontal phase velocities and amplitudes of the CTIDs at 200 and 300 km altitude are different. The horizontal phase velocities at 300 km altitude are slightly greater than those at 200 km, but the difference between them is not significant. Similar observations were also reported in the research of Hurricane Matthew [31]. Vadas [49] suggested that GWs with larger horizontal phase velocities and smaller amplitudes were more likely to propagate to higher thermosphere. In addition, several studies indicated that higher ionospheric altitudes with elevated neutral temperatures may result in atmospheric waves induced TIDs to exhibit larger propagation velocities [29], [50].

In addition to the horizontal phase velocity of CTIDs, 3-DCIT also captured their vertical phases. The vertical slices of dNe show U-shaped structures and are typically observed at lower ionospheric altitudes. Similarly, the simulations of Lamb waves

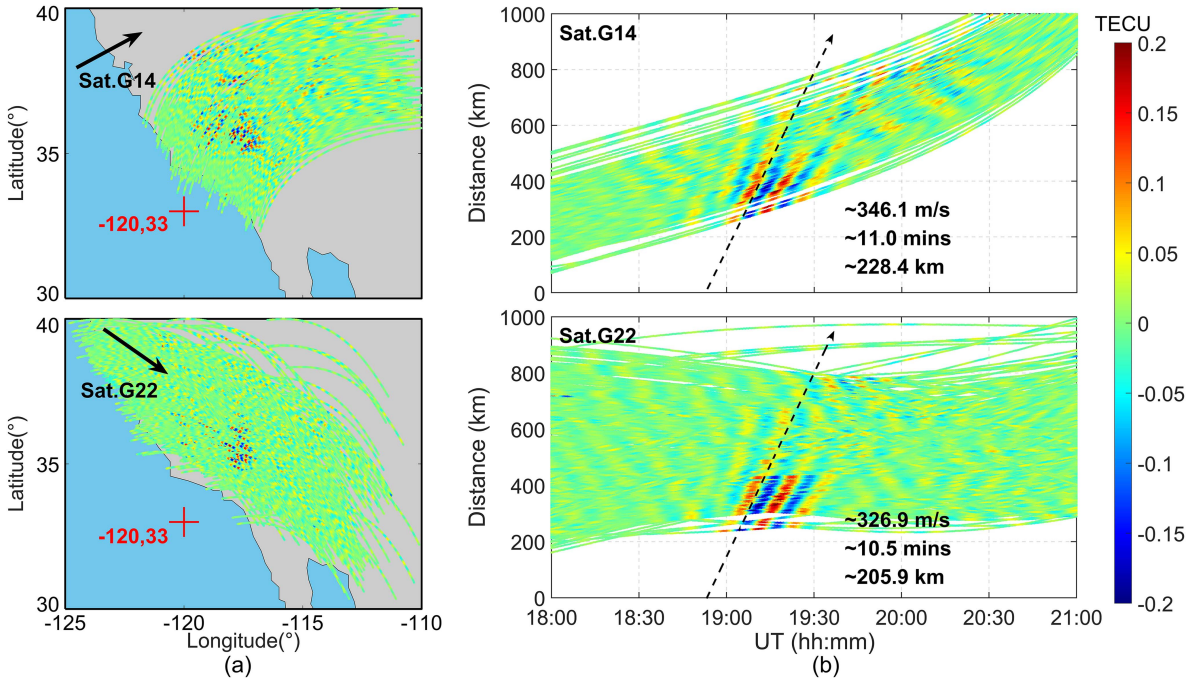

Fig. 11. (a) dVTEC on the IPP trajectories at 350 km altitude for satellites G14 and G22. Arrows indicate the direction of IPP trajectory motion, and the red cross markers indicate the reference point (−120, 33). (b) Time–distance–dVTEC plots relative to the reference point. Dashed arrows show the horizontal phase velocities of the disturbances, with corresponding periods and horizontal wavelengths indicated.

induced by the 2022 Tonga volcano eruption indicate that the vertical phase of CTIDs exhibits a remarkable outward tilt above 300 km altitude [51], [52]. As GWs travel upwards, the acceleration of the background wind due to dissipation increases the phase velocities. However, as the velocities increase, GWs spend less time in the background, leading to a reduction in dissipation and a suppression of acceleration, resulting in a U-shaped structure. In Fig. 9, the inclination changes of the disturbances are small at altitudes of 200 and 300 km, making the differences in the estimated horizontal phase velocities not significant. Like horizontal phase velocity, the vertical phase velocity of GWs also increases since the neutral temperature increases significantly with altitudes. Moreover, the GWs can also exhibit self-acceleration behavior in the vertical direction [53], causing CTIDs at higher altitudes to have larger vertical phase velocities, as seen in Fig. 10. This observation is consistent with the radar plot of postsunrise GW induced ionospheric perturbations in Zhang et al. [9], which also reveals similar vertical velocity differences. When the vertical acceleration is much greater than the horizontal acceleration, it is more conducive to the formation of U-shaped structures. In addition, the propagation of GWs to MLT and higher altitudes depends on their amplitudes, scales, phase velocities, as well as the prevailing wind and temperature fields. Fritts et al. [54] suggested that GWs with small phase velocities and vertical wavelengths may experience unfavorable wind fields and critical layers, resulting in dissipation at lower altitudes. In Fig. 10, it is observed that CTIDs in the 30° and 105° azimuths directions exhibit larger vertical wavelengths and propagate to higher altitudes. However, the evolution of GWs is influenced by multiple factors and is a complex process. The coupling process of neutral atmospheric oscillations from the troposphere to the mesosphere, then to ionosphere still needs to be described by comprehensive observation and simulation data.

Furthermore, the possibility of incorporating GNSS radio occultation (GNSS-RO) data into 3-DCIT modeling to complement ground observations was explored. However, compared to the continuous 30-s interval sampling of GNSS ground-based observations, the shorter sampling duration poses challenges when using a bandpass filter to capture the TIDs. As the measurement time of GNSS-RO STEC profile is ∼1–2 min, which is much shorter than the periods (∼11–15 min) of GWs-induced TIDs [55], [56]. Some studies utilized the constellation observing system for meteorology, ionosphere, and climate [57] or broadband emission radiometry temperature profiles [58] only to detect 1-D ionospheric disturbances but could not obtain 3-D TIDs with wave characteristics due to the lower spatial and temporal resolutions.

VI. Conclusion

This article investigated the 4-D evolution of CTIDs induced by the Falcon 9 rocket launch on 17 January 2016 using 3-DCIT involving dSTEC as follows.

1) Remarkable ionospheric disturbances were detected ∼10–20 min after the rocket launch. Spectral analysis of GNSS observations indicated that the disturbances had frequencies of 1–2 mHz and amplitudes of 0.15–0.25 TECU.
2) These disturbances present nice concentric rings, which were prominently observed between altitudes of 200 and 300 km. The northward propagating CTIDs had larger horizontal phase velocities (∼309.9–323.3 m/s at 200 km

altitude, ∼309.4–330.9 m/s at 300 km altitude) than eastward propagating CTIDs (∼223.2 m/s at 200 km altitude, ∼241.1 m/s at 300 km altitude).

3) The CTIDs exhibited U-shaped structures in their vertical profiles, with inclination angles corresponding to the vertical phase velocities. Between altitudes of 100–200 km, the vertical phase velocities of CTIDs ranged from ∼208.3 to ∼242.4 m/s, while at altitudes exceeding 400 km, the vertical phase velocities reached ∼566.7–944.4 m/s.

Such CTID spatiotemporal characteristics can be incorporated into the GW theory to understand the relationship between the troposphere and ionosphere, as well as the ion-neutral coupling processes. In future articles, independent observations of the lower atmosphere are still necessary to provide a comprehensive evolution process of GWs. Meanwhile, during the iterative process of 3-DCIT, integrating observations from low Earth orbit satellites, cubesats, and ionosondes to provide more reliable initial values is a promising method for improving the reconstruction accuracy.

Acknowledgment

The authors would like to thank the Scripps Orbit and Permanent Array Center, Atmospheric Administration CORS Network for providing GNSS rinex data, and the National Aeronautics and Space Administration for providing solar and geomagnetic indices.

References

[1] J. Yue, L. Hoffmann, and M. J. Alexander, "Simultaneous observations of convective gravity waves from a ground-based airglow imager and the AIRS satellite experiment," *J. Geophys. Res.: Atmos.*, vol. 118, no. 8, pp. 3178–3191, 2013, doi: 10.1002/jgrd.50341.

[2] J. Kong et al., "A clear link connecting the troposphere and ionosphere: Ionospheric responses to the 2015 Typhoon Dujuan," *J. Geodesy*, vol. 91, no. 9, pp. 1087–1097, Sep. 2017, doi: 10.1007/s00190-017-1011-4.

[3] C. J. Heale, J. B. Snively, A. N. Bhatt, L. Hoffmann, C. C. Stephan, and E. A. Kendall, "Multilayer observations and modeling of thunderstorm-generated gravity waves over the midwestern United States," *Geophys. Res. Lett.*, vol. 46, no. 23, pp. 14164–14174, 2019, doi: 10.1029/2019gl085934.

[4] S. L. Vadas and G. Crowley, "Sources of the traveling ionospheric disturbances observed by the ionospheric TIDDBIT sounder near Wallops Island on 30 October 2007," *J. Geophys. Res.: Space Phys.*, vol. 115, 2010, Art. no. A07324, doi: 10.1029/2009ja015053.

[5] M. Nishioka, T. Tsugawa, M. Kubota, and M. Ishii, "Concentric waves and short-period oscillations observed in the ionosphere after the 2013 Moore EF5 tornado," *Geophys. Res. Lett.*, vol. 40, no. 21, pp. 5581–5586, Nov. 16, 2013, doi: 10.1002/2013gl057963.

[6] L. M. Rolland, P. Lognonné, and H. Munekane, "Detection and modeling of Rayleigh wave induced patterns in the ionosphere," *J. Geophys. Res.: Space Phys.*, vol. 116, 2011, Art. no. A05320, doi: 10.1029/2010ja016060.

[7] J. Artru, V. Ducic, H. Kanamori, P. Lognonné, and M. Murakami, "Ionospheric detection of gravity waves induced by tsunamis," *Geophys. J. Int.*, vol. 160, no. 3, pp. 840–848, 2005, doi: 10.1111/j.1365-246X.2005.02552.x.

[8] D. R. Themens et al., "Global propagation of ionospheric disturbances associated with the 2022 Tonga volcanic eruption," *Geophys. Res. Lett.*, vol. 49, 2022, Art. no. e2022GL098158, doi: 10.1029/2022gl098158.

[9] S. R. Zhang et al., "Electrified postsunrise ionospheric perturbations at Millstone Hill," *Geophys. Res. Lett.*, vol. 48, no. 18, 2021, Art. no. e2021GL095151, doi: 10.1029/2021gl095151.

[10] P. R. Arendt, "Ionospheric undulations following Apollo 14 launching," *Nature*, vol. 231, no. 5303, pp. 438–439, 1971, doi: 10.1038/231438a0.

[11] E. Calais and J. B. Minster, "GPS detection of ionospheric perturbations following a space shuttle ascent," *Geophys. Res. Lett.*, vol. 23, no. 15, pp. 1897–1900, 1996, doi: 10.1029/96gl01256.

[12] S. T. Noble, "A large-amplitude traveling ionospheric disturbance excited by the space shuttle during launch," *J. Geophys. Res.: Space Phys.*, vol. 95, no. A11, pp. 19037–19044, 1990, doi: 10.1029/JA095iA11p19037.

[13] A. R. Jacobson and R. C. Carlos, "Observations of acoustic-gravity waves in the thermosphere following Space Shuttle ascents," *J. Atmos. Terr. Phys.*, vol. 56, no. 4, pp. 525–528, 1994, doi: 10.1016/0021-9169(94)90201-1.

[14] Y. Q. Li, A. R. Jacobson, R. C. Carlos, R. S. Massey, Y. N. Taranenko, and G. Wu, "The blast wave of the Shuttle plume at ionospheric heights," *Geophys. Res. Lett.*, vol. 21, no. 24, pp. 2737–2740, 1994, doi: 10.1029/94gl02548.

[15] T. Liu, B. Zhang, Y. Yuan, and X. Zhang, "On the application of the raw-observation-based PPP to global ionosphere VTEC modeling: An advantage demonstration in the multi-frequency and multi-GNSS context," *J. Geodesy*, vol. 94, no. 1, pp. 1–20, 2019, doi: 10.1007/s00190-019-01332-z.

[16] X. Ren, J. Chen, X. Zhang, M. Schmidt, X. Li, and J. Zhang, "Mapping topside ionospheric vertical electron content from multiple LEO satellites at different orbital altitudes," *J. Geodesy*, vol. 94, no. 9, pp. 1–17, 2020, doi: 10.1007/s00190-020-01415-2.

[17] X. Gao and Y. Yao, "A storm-time ionospheric TEC model with multichannel features by the spatiotemporal ConvLSTM network," *J. Geodesy*, vol. 97, no. 1, 2023, Art. no. 9, doi: 10.1007/s00190-022-01696-9.

[18] T. Bowling, E. Calais, and J. S. Haase, "Detection and modelling of the ionospheric perturbation caused by a Space Shuttle launch using a network of ground-based Global Positioning System stations," *Geophys. J. Int.*, vol. 192, no. 3, pp. 1324–1331, 2013, doi: 10.1093/gji/ggs101.

[19] L. M. He, L. X. Wu, S. J. Liu, and S. N. Liu, "Superimposed disturbance in the ionosphere triggered by spacecraft launches in China," *Annales Geophysicae*, vol. 33, no. 11, pp. 1361–1368, 2015, doi: 10.5194/angeo-33-1361-2015.

[20] C. H. Lin et al., "Ionospheric shock waves triggered by rockets," *Annales Geophysicae*, vol. 32, no. 9, pp. 1145–1152, 2014, doi: 10.5194/angeo-32-1145-2014.

[21] F. Ding et al., "Ionospheric response to the shock and acoustic waves excited by the launch of the Shenzhou 10 spacecraft," *Geophys. Res. Lett.*, vol. 41, no. 10, pp. 3351–3358, 2014, doi: 10.1002/2014gl060107.

[22] Y. Kakinami et al., "Ionospheric disturbances induced by a missile launched from North Korea on 12 December 2012," *J. Geophys. Res.: Space Phys.*, vol. 118, no. 8, pp. 5184–5189, 2013, doi: 10.1002/jgra.50508.

[23] C. C. H. Lin et al., "Concentric traveling ionospheric disturbances triggered by the launch of a SpaceX Falcon 9 rocket," *Geophys. Res. Lett.*, vol. 44, no. 15, pp. 7578–7586, Aug. 16, 2017, doi: 10.1002/2017gl074192.

[24] M.-Y. Chou, C. C. H. Lin, M.-H. Shen, J. Yue, J. D. Huba, and C.-H. Chen, "Ionospheric disturbances triggered by SpaceX Falcon Heavy," *Geophys. Res. Lett.*, vol. 45, no. 13, pp. 6334–6342, 2018, doi: 10.1029/2018gl078088.

[25] D. Zheng, Y. Yao, W. Nie, N. Chu, D. Lin, and M. Ao, "A new three-dimensional computerized ionospheric tomography model based on a neural network," *GPS Solutions*, vol. 25, no. 1, pp. 1–17, 2020, doi: 10.1007/s10291-020-01047-1.

[26] J. Kong, F. Li, Y. Yao, Z. Wang, W. Peng, and Q. Zhang, "Reconstruction of 2D/3D ionospheric disturbances in high-latitude and arctic regions during a geomagnetic storm using GNSS carrier TEC: A case study of the 2015 great storm," *J. Geodesy*, vol. 93, no. 9, pp. 1529–1541, 2019, doi: 10.1007/s00190-019-01266-6.

[27] C. Zhai et al., "3-D tomographic reconstruction of SED plume during 17 March 2013 storm," *J. Geophys. Res.: Space Phys.*, vol. 125, no. 11, 2020, Art. no. e2020JA028257, doi: 10.1029/2020ja028257.

[28] N. Ssessanga, Y. H. Kim, and E. Kim, "Vertical structure of medium-scale traveling ionospheric disturbances," *Geophys. Res. Lett.*, vol. 42, no. 21, pp. 9156–9165, 2015, doi: 10.1002/2015gl066093.

[29] C. Zhai, Y. Yao, and J. Kong, "Three-dimensional reconstruction of seismo-traveling ionospheric disturbances after March 11, 2011, Japan Tohoku earthquake," *J. Geodesy*, vol. 95, no. 7, 2021, Art. no. 77, doi: 10.1007/s00190-021-01533-5.

[30] J. Kong et al., "Tridimensional reconstruction of the Co-Seismic Ionospheric Disturbance around the time of 2015 Nepal earthquake," *J. Geodesy*, vol. 92, no. 11, pp. 1255–1266, 2018, doi: 10.1007/s00190-018-1117-3.

[31] Y. Chen, D. Yue, C. Zhai, and S. R. Zhang, "Detection and three-dimensional reconstruction of concentric traveling ionosphere disturbances induced by Hurricane Matthew on 7 October 2016," *J. Geophys. Res.: Space Phys.*, vol. 127, no. 12, 2022, Art. no. e2022JA030690, doi: 10.1029/2022ja030690.
[32] S. Gu, C. Shi, Y. Lou, and J. Liu, "Ionospheric effects in uncalibrated phase delay estimation and ambiguity-fixed PPP based on raw observable model," *J. Geodesy*, vol. 89, no. 5, pp. 447–457, 2015, doi: 10.1007/s00190-015-0789-1.
[33] M. Y. Chou et al., "Concentric traveling ionosphere disturbances triggered by Super Typhoon Meranti (2016)," *Geophys. Res. Lett.*, vol. 44, no. 3, pp. 1219–1226, Feb. 16, 2017, doi: 10.1002/2016gl072205.
[34] J. T. Lin et al., "Rapid conjugate appearance of the giant ionospheric lamb wave signatures in the Northern hemisphere after Hunga-Tonga volcano eruptions," *Geophys. Res. Lett.*, vol. 49, no. 8, 2022, Art. no. e2022GL098222, doi: 10.1029/2022gl098222.
[35] K. Heki, "Ionospheric signatures of repeated passages of atmospheric waves by the 2022 Jan. 15 Hunga Tonga-Hunga Ha'apai eruption detected by QZSS-TEC observations in Japan," *Earth Planets Space*, vol. 74, no. 1, pp. 1–12, 2022, doi: 10.1186/s40623-022-01674-7.
[36] R. Song, X. Zhang, C. Zhou, J. Liu, and J. He, "Predicting TEC in China based on the neural networks optimized by genetic algorithm," *Adv. Space Res.*, vol. 62, no. 4, pp. 745–759, 2018, doi: 10.1016/j.asr.2018.03.043.
[37] S. Xu et al., "Dynamical coupling between Hurricane Matthew and the middle to upper atmosphere via gravity waves," *J. Geophys. Res.: Space Phys.*, vol. 124, no. 5, pp. 3589–3608, May 2019, doi: 10.1029/2018ja026453.
[38] L. M. Rolland et al., "The resonant response of the ionosphere imaged after the 2011 off the Pacific coast of Tohoku Earthquake," *Earth Planets Space*, vol. 63, no. 7, pp. 853–857, 2011, doi: 10.5047/eps.2011.06.020.
[39] M. Y. Chou, C. C. H. Lin, J. Yue, L. C. Chang, H. F. Tsai, and C. H. Chen, "Medium-scale traveling ionospheric disturbances triggered by Super Typhoon Nepartak (2016)," *Geophys. Res. Lett.*, vol. 44, no. 15, pp. 7569–7577, Aug. 16, 2017, doi: 10.1002/2017gl073961.
[40] P. A. Bernhardt, J. D. Huba, E. Kudeki, R. F. Woodman, L. Condori, and F. Villanueva, "Lifetime of a depression in the plasma density over Jicamarca produced by space shuttle exhaust in the ionosphere," *Radio Sci.*, vol. 36, no. 5, pp. 1209–1220, 2001, doi: 10.1029/2000rs002434.
[41] M. Mendillo, G. S. Hawkins, and J. A. Klobuchar, "A sudden vanishing of the ionospheric region due to the launch of Skylab," *J. Geophys. Res.*, vol. 80, no. 16, pp. 2217–2228, 1975, doi: 10.1029/JA080i016p02217.
[42] G. Savastano et al., "Advantages of geostationary satellites for ionospheric anomaly studies: Ionospheric plasma depletion following a rocket launch," *Remote Sens.*, vol. 11, no. 14, 2019, Art. no. 1734, doi: 10.3390/rs11141734.
[43] M. Y. Chou, J. Yue, C. C. H. Lin, P. K. Rajesh, and N. M. Pedatella, "Conjugate effect of the 2011 Tohoku reflected tsunami-driven gravity waves in the ionosphere," *Geophys. Res. Lett.*, vol. 49, no. 3, 2022, Art. no. e2021GL097170, doi: 10.1029/2021gl097170.
[44] S. L. Vadas, J. Yue, C.-Y. She, P. A. Stamus, and A. Z. Liu, "A model study of the effects of winds on concentric rings of gravity waves from a convective plume near Fort Collins on 11 May 2004," *J. Geophys. Res.: Atmos.*, vol. 114, Art. no. D06103, doi: 10.1029/2008jd010753.
[45] S. L. Vadas and H. L. Liu, "Numerical modeling of the large-scale neutral and plasma responses to the body forces created by the dissipation of gravity waves from 6 h of deep convection in Brazil," *J. Geophys. Res.: Space Phys.*, vol. 118, no. 5, pp. 2593–2617, 2013, doi: 10.1002/jgra.50249.
[46] S. L. Vadas and I. Azeem, "Concentric secondary gravity waves in the thermosphere and ionosphere over the continental United States on March 25–26, 2015 from deep convection," *J. Geophys. Res.: Space Phys.*, vol. 126, no. 2, 2021, Art. no. e2020JA028275, doi: 10.1029/2020ja028275.
[47] J. Liu, R. Chen, J. An, Z. Wang, and J. Hyyppa, "Spherical cap harmonic analysis of the Arctic ionospheric TEC for one solar cycle," *J. Geophys. Res.: Space Phys.*, vol. 119, no. 1, pp. 601–619, 2014, doi: 10.1002/2013ja019501.
[48] I. Zakharenkova, E. Astafyeva, and I. Cherniak, "GPS and GLONASS observations of large-scale traveling ionospheric disturbances during the 2015 St. Patrick's Day storm," *J. Geophys. Res.: Space Phys.*, vol. 121, no. 12, pp. 12,138–12,156, 2016, doi: 10.1002/2016ja023332.
[49] S. L. Vadas, "Horizontal and vertical propagation and dissipation of gravity waves in the thermosphere from lower atmospheric and thermospheric sources," *J Geophys. Res. Space Phys.*, vol. 112, 2007, Art. no. A06305, doi: 10.1029/2006ja011845.
[50] L. Liu, Y. J. Morton, P. H. Cheng, A. Amores, C. J. Wright, and L. Hoffmann, "Concentric traveling ionospheric disturbances (CTIDs) triggered by the 2022 Tonga volcanic eruption," *J. Geophys. Res.: Space Phys.*, vol. 128, no. 2, 2023, Art. no. e2022JA030656, doi: 10.1029/2022ja030656.
[51] H. L. Liu, W. Wang, J. D. Huba, P. H. Lauritzen, and F. Vitt, "Atmospheric and ionospheric responses to Hunga—Tonga volcano eruption simulated by WACCM-X," *Geophys. Res. Lett.*, vol. 50, no. 10, 2023, Art. no. e2023GL103682, doi: 10.1029/2023gl103682.
[52] J. D. Huba, E. Becker, and S. L. Vadas, "Simulation study of the 15 January 2022 Tonga event: Development of super equatorial plasma bubbles," *Geophys. Res. Lett.*, vol. 50, no. 1, 2023, Art. no. e2022GL101185, doi: 10.1029/2022gl101185.
[53] D. C. Fritts, W. Dong, T. S. Lund, S. Wieland, and B. Laughman, "Self-acceleration and instability of gravity wave packets: 3. Three-dimensional packet propagation, secondary gravity waves, momentum transport, and transient mean forcing in tidal winds," *J. Geophys. Res.: Atmos.*, vol. 125, no. 3, Feb. 16 2020, Art. no. e2019JD030692, doi: 10.1029/2019JD030692.
[54] D. C. Fritts, B. Laughman, L. Wang, T. S. Lund, and R. L. Collins, "Gravity wave dynamics in a mesospheric inversion layer: 1. Reflection, trapping, and instability dynamics," *J. Geophys. Res. Atmos.*, vol. 123, no. 2, pp. 626–648, Jan. 27, 2018, doi: 10.1002/2017JD027440.
[55] G. Savastano, K. Nordström, and M. J. Angling, "Semi-supervised classification of lower-ionospheric perturbations using GNSS radio occultation observations from Spire Global's Cubesat Constellation," *J. Space Weather Space Climate*, vol. 12, 2022, Art. no. 14, doi: 10.1051/swsc/2022009.
[56] P. Alexander, A. de la Torre, and P. Llamedo, "Interpretation of gravity wave signatures in GPS radio occultations," *J. Geophys. Res.: Atmos.*, vol. 113, 2008, Art. no. D16117, doi: 10.1029/2007jd009390.
[57] N. Ssessanga, Y. H. Kim, and S. H. Jeong, "A statistical study on the F2 layer vertical variation during nighttime medium-scale traveling ionospheric disturbances," *J. Geophys. Res.: Space Phys.*, vol. 122, no. 3, pp. 3586–3601, 2017, doi: 10.1002/2016ja023463.
[58] X. Liu, J. Xu, J. Yue, and M. Kogure, "Strong gravity waves associated with Tonga volcano eruption revealed by SABER observations," *Geophys. Res. Lett.*, vol. 49, no. 10, 2022, Art. no. e2022GL098339, doi: 10.1029/2022gl098339.

Yutian Chen received the B.S. degree in surveying and mapping engineering from the Shanxi Datong University, Datong, China, in 2016, and the M.S. degree in surveying and mapping from the Guilin University of Technology, Guilin, China, in 2019. He is currently working toward the Ph.D. degree in geodesy with the School of Earth Sciences and Engineering, Hohai University, Nanjing, China.

His research interests include ionospheric detection, upper atmosphere research, and GNSS data processing.

Dongjie Yue received the M.S. and Ph.D. degrees in surveying and mapping from the Hohai University, Nanjing, China, in 1994 and 2005, respectively.

She is currently a Full Professor with the School of Earth Sciences and Engineering, Hohai University. Her research interests include satellite navigation and positioning, GNSS data processing, precision engineering measurement, and engineering deformation monitoring.

Changzhi Zhai received the B.S. degree in surveying and mapping engineering from the Hohai University, Nanjing, China, in 2014, and the M.S and Ph.D. degrees in geodesy from the Wuhan University, Wuhan, China, in 2017 and 2020, respectively.

His research interests include GNSS data processing, ionospheric disturbance detection, and space physics research.